

Demonstration of algorithmic quantum speedup

Bibek Pokharel^{1,2,*} and Daniel A. Lidar^{1,2,3,4,†}

¹*Department of Physics & Astronomy*

²*Center for Quantum Information Science & Technology*

³*Department of Electrical & Computer Engineering*

⁴*Department of Chemistry*

University of Southern California, Los Angeles, CA 90089, USA

(Dated: July 18, 2022)

Quantum algorithms theoretically outperform classical algorithms in solving problems of increasing size [1–5], but computational errors must be kept to a minimum to realize this potential. Despite the development of increasingly capable quantum computers (QCs), an experimental demonstration of a provable algorithmic quantum speedup [6] employing today’s non-fault-tolerant, noisy intermediate-scale quantum (NISQ) [7] devices has remained elusive. Here, we unequivocally demonstrate such a speedup, quantified in terms of the scaling with the problem size of the time-to-solution metric. We implement the single-shot Bernstein-Vazirani algorithm, which solves the problem of identifying a hidden bitstring that changes after every oracle query, utilizing two different 27-qubit IBM Quantum (IBMQ) [8] superconducting processors. The speedup is observed on only one of the two QCs (ibmq_montreal) when the quantum computation is protected by dynamical decoupling (DD) – a carefully designed sequence of pulses applied to the QC that suppresses its interaction with the environment [9, 10], but not without DD. In contrast to recent quantum supremacy demonstrations [11–13], the quantum speedup reported here does not rely on any additional assumptions or complexity-theoretic conjectures [14–16] and solves a bona fide computational problem, in the setting of a game with an oracle and a verifier.

Main

The quest to demonstrate a quantum speedup for a computational problem, i.e., an algorithmic quantum speedup, has motivated the field of quantum computing from its inception. Early theoretical breakthroughs, most notably Shor’s factorization algorithm [4], set in motion a remarkable surge of quantum hardware development aimed at realizing the potential of a quantum speedup. The last several years have witnessed the deployment of both academic and commercial quantum computing platforms accessible to experimentation via the cloud. Better-than-classical algorithmic performance has been demonstrated a number of times, e.g., on ion-trap [17, 18], superconducting [19, 20], photonic [21–24], and Rydberg atom [25] quantum processors, in most cases by exceeding the corresponding classical algorithmic success probability at a fixed problem size, or a small set of such sizes.

However, as we explain in more detail below, this does not yet amount to an algorithmic quantum speedup demonstration, which involves the more stringent criterion of the scaling with problem size of the time-to-solution metric. We provide a comprehensive survey of existing experimental demonstrations of better-than-classical algorithmic results in Appendix A.

To qualify as a genuine, *provable* algorithmic quantum speedup, we insist that the speedup be relative to a problem whose classical solution cannot be improved in principle and is unconditional over the range of accessible problem sizes. In other words, the scaling advantage of the time-to-solution does not rely on any assumptions and persists up to the largest number of qubits compatible with the QC being used to demonstrate it. To satisfy this stringent notion of an algorithmic quantum speedup, we revisit the Bernstein-Vazirani (BV) algorithm, which was one of the very first theoretical examples of a quantum speedup and quantum/classical complexity class separation [2]. In the original BV problem, an oracle outputs $f_b(x) = b \cdot x \pmod{2}$, where x and b are both length- n bitstrings. Here x is a guess provided by the user and b is a secret bitstring the user is trying to learn in as few oracle queries as possible. The best classical algorithm requires n queries of the type $f_b(0 \dots 01_i 0 \dots 0)$, $i \in \{1, 2, \dots, n\}$, each of which returns one unknown bit $b_i \in b$. By solving the problem with certainty in a *single* query, the BV algorithm provides a linear speedup over the best-classical algorithm.

Here we consider a modified, single-shot version of BV, denoted ssBV- n , where the hidden bitstring b changes after every query [see Fig. 1(top)]. We colloquially refer to this as the “BV guessing game”: after one query of the single-shot oracle, the player is allowed one guess of the bitstring b . If the verifier confirms that the guess is correct, the player wins; if the guess is wrong, the game continues with a new oracle encoding a new bitstring.

In this setting, the best classical algorithm is to each time query the oracle with bitstring $0 \dots 01_i 0 \dots 0$ (i is arbitrary), which reveals b_i , and then guess the remaining $n - 1$ bits. This yields classical success probability $p_s = 2^{1-n}$, only twice better than a random guess. In stark contrast, a player with access to a QC running the original BV algorithm has success probability $p_s = 1$ after each query, which becomes an exponential advantage in the speedup ratio (defined below) over the classical setting.

Quantum speedup quantified

In a head-to-head comparison of success probabilities, $p_s >$

* pokharel@usc.edu

† lidar@usc.edu

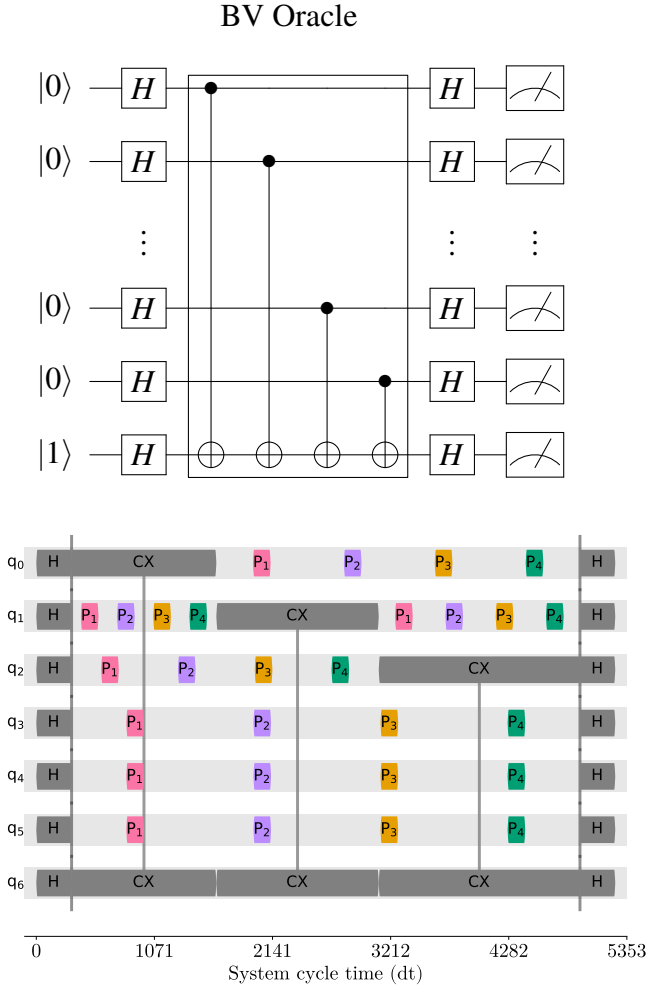


FIG. 1. Top: Circuit for the BV algorithm with the unknown bit-string $b = 1 \dots 1$. In the BV guessing game (or ssBV- n problem), the oracle changes after each circuit execution and encodes a new bit-string b . Note that the internal structure of the circuit is hidden from the player, so the fact that the BV circuit can be efficiently simulated classically (since it uses only Clifford gates [26]) is immaterial. Each BV- n circuit requires $n + 1$ qubits and a circuit of depth $\geq n + 3$ (with equality only for fully connected architectures). A controlled-NOT (CNOT) or identity gate is performed from qubit i to the ancilla qubit if $b_i = 1$ or 0 , respectively. Bottom: The same circuit for BV-6 with DD pulses during idle times; P_i denotes pulses. Pulse placement is schematic but illustrates all the principles we used in practice: (i) DD fills all available idle spaces, (ii) pulse intervals are varied depending on the available idle time per qubit, (iii) pulse types can differ (i.e., $P_i \neq P_j$), (iv) a single qubit experiences multiple repetitions of a sequence if there are disjoint intervals (as in the case of q_1). The actual timeline is shown, in units of $dt = 2/9$ ns – the inverse sampling rate of the backend’s arbitrary waveform generators.

2^{1-n_0} , for a fixed problem size n_0 , implies a better-than-classical result. This is the context in which better-than-classical results have been achieved for the Grover and BV algorithms [17–19]. However, the success probability at fixed problem size is not a reliable measure of quantum speedup, as detecting an algorithmic speedup requires the scaling with

problem size. Moreover, p_s is itself a function of the time $t_r(n)$ taken to run the calculation, i.e., the time required to run the complete quantum or classical circuit once. Instead, we quantify quantum speedup in terms of the scaling with the problem size n of the speedup ratio of the classical and quantum total runtimes: $S(n) = \frac{\text{TTS}_C(n)}{\text{TTS}_Q(n)}$, where the total runtime is quantified using the well-established time-to-solution (TTS) metric [6]:

$$\text{TTS}(n) = t_r(n)R(n), \quad R(n) = \frac{\log(1 - p_d)}{\log(1 - p_s(t_r(n)))}. \quad (1)$$

$[R(n)]$ is the number of repetitions – oracle calls in the present context – needed to find a solution at least once with desired probability p_d , given that a single repetition succeeds with probability $p_s(t_r(n))$; we set $p_d = 0.99$ henceforth. Thus, the TTS quantifies the total time it takes to win the BV guessing game, whether classically or with access to a QC.

We choose to measure $t_r(n)$ in terms of the circuit execution time and the readout duration, and ignore precompilation and postprocessing overheads, as the latter are inherently classical. It follows from the BV circuit structure (Fig. 1) that $t_r(n) = c\tau_{2q}n + \tau_0$, where $1 \leq c \leq 2$ depends on the qubit connectivity graph, with the two limits corresponding to all-to-all connectivity ($c = 1$) and a chain ($c = 2$). For our IBMQ implementation, we found $c \approx 1.76$ (see Appendix D for more details). The two-qubit gate time, τ_{2q} , and the sum of the single qubit and readout times, τ_0 , depend on the specific QC and can differ by orders of magnitude across platforms; e.g., τ_{2q} is measured in microseconds for trapped-ion qubits and nanoseconds for superconducting qubits.

Let n_{\max} denote the largest number of data qubits available to a quantum algorithm; e.g., in the BV algorithm case, which requires one ancilla qubit, $n_{\max} = n_{\text{tot}} - 1$, where n_{tot} is the total number of programmable physical qubits available on the physical quantum device. Any scaling of $S(n)$ that is extracted from a QC with a relatively small n_{tot} , as is invariably the case in the current NISQ era [7], is naturally subject to finite-size effects. Thus, the best one can hope for is that extrapolations to $n > n_{\max}$ are meaningful, and any conclusions based on such extrapolations must be revisited when devices with larger n_{tot} become available. With this in mind, we estimate the scaling of the speedup ratio $S(n)$ by computing the most conservative estimate allowed by the experimental data, as explained below. This extrapolated scaling can be used to compare different QCs.

In the ssBV- n case, we expect $\text{TTS}_Q(n)$ to scale as $n2^{\lambda n}$ (with $\lambda > 0$) due to decoherence, instead of as $t_r \sim n$, as would be the case for a noiseless QC. When ssBV- n is solved classically, computing $f_b(x) = b \cdot x \pmod{2}$ also takes time $\propto n$ (the cost of adding n bits), so we obtain $\text{TTS}_C(n) \propto n / \log_2(1 - 2^{1-n}) \approx n2^{n-1}$. We thus expect

$$S(n) \sim 2^{(1-\lambda)n}, \quad n \in [n_{\min}, n_{\max}], \quad (2)$$

where n_{\min} is identified empirically by excluding small-size effects. We will declare a quantum speedup if the speedup exponent $\lambda < 1$. It is important to emphasize that the speedup exponent must be extracted using n reaching up to and including n_{\max} , since otherwise one cannot hope to

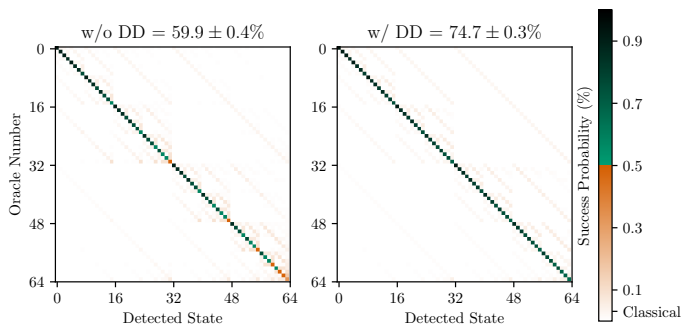


FIG. 2. Full output distribution for BV-6 from Cairo. Oracles f_b are numbered from 0 to 63, corresponding to $b \in \{0^6, \dots, 1^6\}$. Ideally, the output state for oracle f_b (vertical axis) is b , but in reality, other bitstrings (horizontal axis) are observed as well. Green dots on the diagonal correspond to $p_s > 1/2$, where p_s is the empirical frequency (success probability) with which b was output for oracle f_b . Without DD, the average success probability over all oracles is $59.9 \pm 0.4\%$, but for some oracles, $p_s < 1/2$. With DD, the average success probability rises to $74.7 \pm 0.3\%$ and $p_s > 1/2$ for all oracles. Success probabilities are reported with 5σ confidence intervals.

draw conclusions that reflect asymptotic scaling behavior. Using this criterion, we demonstrate below that a statistically significant quantum speedup is achieved for DD-protected ssBV- n quantum circuits, but no speedup is obtained for “bare” quantum circuits implemented without DD.

Dynamical decoupling

DD-protection has a long history of experimental demonstrations on various quantum devices (see Ref. [10] for a review), and has also been shown to improve various performance metrics, such as qubit memory fidelity [27, 28], crosstalk mitigation [29], quantum volume [30], and algorithmic fidelity [31]. Various theoretical strategies for how to combine DD with quantum computation have been described [32–34], but we are unaware of prior experimental demonstrations of the use of DD to directly improve quantum algorithmic scaling.

We employ a “decouple then compute” strategy [35, 36], whereby DD control pulses constituting short but complete DD sequences are interleaved with the quantum circuit by exploiting intervals when individual qubits in the corresponding quantum circuits are idle; see Fig. 1(bottom).

A major challenge in using DD is that pulse imperfections can significantly deteriorate performance, necessitating a careful choice of DD sequence. Building on a survey of numerous known sequences [37], we selected the universally robust (UR) sequence family [38] as the top performance enhancer. This sequence was designed to suppress flip-angle errors and has been shown previously to enhance performance in superconducting-qubit-based NISQ devices [28, 39].

Experimental implementation

We implemented ssBV- n on two different 27-qubit QCs: `ibmq_montreal` and `ibmq_cairo` (henceforth Montreal and Cairo). Considering that one qubit must function as the ancilla in the BV algorithm, we have $n_{\max} = 26$. These devices fea-

ture fixed-frequency transmon qubits with microwave pulses for implementing control and readout. While similar in their connectivity, they have different quantum volumes, qubit generations, and gate fidelities (see Appendix C for details).

Setting aside connectivity considerations, given the unknown string b the BV oracle is implemented by performing CNOTs from a subset of the first $|b| = n$ qubits to the ancilla qubit (always numbered $n + 1$), preceded and followed by Hadamard gates (see Fig. 1). Whether a CNOT is applied from qubit i to the ancilla is determined by whether $b_i = 0$ (do nothing) or $b_i = 1$ (apply a CNOT). The number of CNOTs is thus the Hamming weight k (the number of 1’s in b). Given n and k , there are $\binom{n}{k}$ distinct bitstrings, and the circuits for all these bitstrings are identical up to qubit permutation. We exploited this symmetry and generally avoided the impractical task of testing $\sum_{k=0}^n \binom{n}{k} = 2^n$ oracles by testing only the $n + 1$ cases $b = 1^k 0^{n-k}$ with $0 \leq k \leq n$ for each n .

Results

BV-6 test results, both with and without DD, are shown in Fig. 2. With DD, for every one of the 2^6 oracles (inputs) tested, the single-shot output success probability exceeds $1/2$, which allows reaching the $2/3$ bounded-error quantum polynomial (BQP) threshold for all possible inputs by classical majority vote on multiple repetitions [2, 18]. Without DD, the single-shot output success probability is below $1/2$ for nearly a third of all inputs (though always higher than the classical single-shot probability of $1/64$), so the BQP threshold cannot be reached. This already suggests that error suppression through DD will be central to our quantum speedup demonstration. However, to genuinely demonstrate a quantum speedup we must demonstrate a scaling advantage with problem size n , which brings us to our central result.

Our main result is presented in Fig. 3, which shows the TTS as a function of problem size n for both Montreal and Cairo. White grid lines show the asymptotic classical TTS [scaling as $O(2^n)$], and the ideal quantum TTS (equal to $t_r(n) \sim n$) is shown for reference by the two dashed lines – one each for Montreal and Cairo. As is apparent visually, the scaling without DD (empty symbols) for both devices is worse than the classical scaling. Moreover, without DD, the success probability drops to zero for $n > 16$ (Montreal) and $n > 20$ (Cairo); hence the TTS curves terminate. We attribute this worse-than-classical scaling at large problem sizes to the fact that transmon-based devices suffer from spontaneous emission errors, as a result of which they preferentially generate bitstrings with low Hamming weight, which is worse than a uniformly random guess. This is also apparent from Fig. 2(left), which exhibits a trend of lower success probabilities for oracles with a higher index and hence higher Hamming weight.

With DD, this problem is mitigated, so that $p_s > 0$ is extended for Cairo (blue) to $n = 23$ (excessive readout noise required us to treat Cairo as a device with $n_{\text{tot}} = 24$; see Appendix C). Most notably, it is clear that with DD the Montreal scaling (orange) is better than classical and extends to $n = n_{\max} = 26$, suggesting a quantum speedup.

To quantify this and extract the speedup exponent λ as

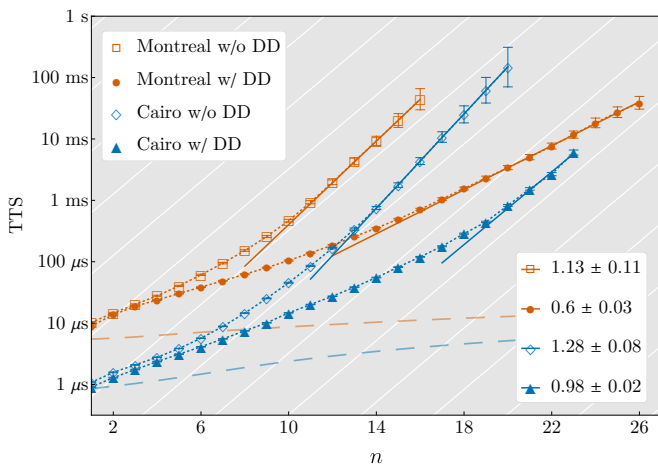


FIG. 3. Time-to-solution (TTS) as a function of problem size or number of data qubits n . Results for Montreal and Cairo are shown by the orange and blue symbols, respectively, and filled (empty) symbols represent results with (without) DD; dotted lines are guides to the eye. The asymptotic classical scaling $TTS_C(n) \sim 2^n$ is shown as white grid lines, and the hypothetical, ideal quantum scaling $TTS_Q(n) \propto n$ of each QC is indicated by the dashed lines (for QC-specific parameter values see Appendix C). The worst-case scaling fit for each curve is shown by the solid lines, whose slopes λ are reported in the bottom legend, with uncertainties representing 95% confidence intervals. Without DD, the TTS results terminate at $n'_{\max} = 16$ ($n'_{\max} = 20$) for Montreal (Cairo) as $p_s = 0$ for $n > n'_{\max}$. Moreover, $\lambda > 1$ without DD, indicating a worse-than-classical scaling. With DD protection, on Cairo, the $p_s > 0$ range is extended to $n = 23$, and λ is just below the breakeven point of 1, but the uncertainty is too large to conclude that quantum speedup has occurred. In contrast, the Montreal scaling with DD does exhibit quantum speedup, as explained in the text. Since two-qubit operations and readout durations are shorter for Cairo, it exhibits a consistently lower absolute TTS than Montreal. We report 5σ confidence intervals from bootstrapping for each data point (see Methods); error bars are mostly covered by the symbols.

conservatively as possible, we compute the worst-case scaling from our data (see Methods). The results are shown as the straight blue and orange lines in Fig. 3, along with the numerical values of λ in the legend. Without DD, we obtain $\lambda = 1.13 \pm 0.11$ and 1.28 ± 0.08 for Montreal and Cairo, respectively, meaning a quantum slowdown. For Cairo, the scaling with DD is $\lambda = 0.98 \pm 0.02$, not a statistically significant difference from the classical scaling. However, the fit confirms that *Montreal with DD exhibits a quantum speedup*: $\lambda = 0.60 \pm 0.03$. All the reported uncertainties represent 2σ symmetric confidence intervals; see Methods. The difference between Cairo and Montreal agrees with the reported larger quantum volume (128 vs 64) of Montreal [40], and suggests that the latter is a relevant performance metric also in the present context of algorithmic speedups.

It is clear from Fig. 3 that all the slopes vary with n . One might thus ask what the scaling would appear to be for a hypothetical QC with fewer qubits (h_{\max}) than the actual $n_{\max} = 26$; we address this in Fig. 4. This figure shows the maximum local slope of each of the curves in Fig. 3 for

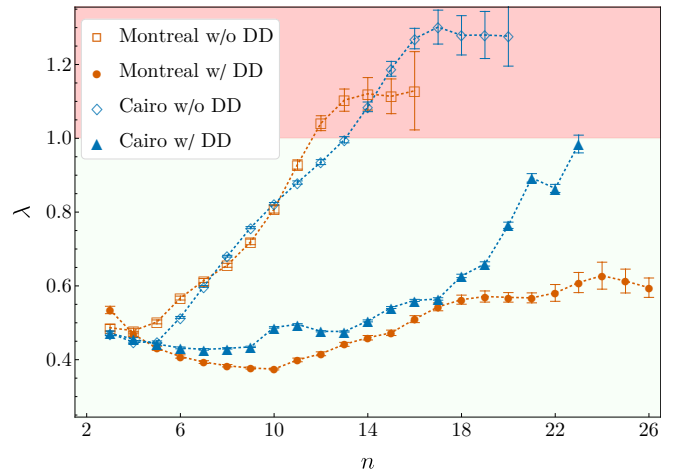


FIG. 4. Results for $\lambda_{h_{\max}}$, the maximum local slope of each of the curves in Fig. 3 for $n \leq h_{\max}$, i.e., the worst-case-scaling when restricted to QC with $h_{\max} + 1$ qubits. Only Montreal with DD exhibits an unambiguous quantum speedup, with $\lambda_{h_{\max}}$ well below 1 for all $n \leq h_{\max}$. Error bars represent 2σ confidence intervals.

$n \leq h_{\max}$ (see Methods). The results clearly show the growth of the speedup exponents $\lambda_{h_{\max}}$ for Cairo with and without DD, and for Montreal without DD, to the point $\lambda > 1$ or beyond, where no quantum speedup survives. In contrast, the speedup exponent for Montreal with DD is well within the quantum speedup region of $\lambda < 1$ for all values of h_{\max} .

Discussion and Conclusions

The ssBV- n problem has a *provable* exponential quantum speedup over the best possible classical algorithm in the setting of a game involving an oracle and a verifier, which makes it an attractive target for an experimental quantum speedup demonstration. The BV algorithm, the key ingredient in our work, is frequently used for benchmarking NISQ devices [18, 19, 41–43], with the largest prior implementations being BV-11 and BV-20 [44] on superconducting and trapped-ion devices respectively. Here we reached BV-26 on a superconducting device (ibmq_montreal), by invoking dynamical decoupling (DD). This corresponds to a maximal circuit depth of 44 CNOTs (46 when accounting for the Hadamard gates at the beginning and end), slightly higher than the largest depth (40) reached in quantum supremacy experiments [11, 12]; see Appendix D.

To test for a quantum speedup, we compared the asymptotic scaling of the TTS metric with problem size for both classical and quantum algorithms. We demonstrated a statistically significant algorithmic quantum speedup on Montreal using this metric. A crucial feature in our implementation was error-suppression through DD, without which the speedup was not exhibited.

It is reasonable to question whether this speedup can be expected to continue indefinitely. In the absence of fault-tolerant quantum error correction [45] decoherence always eventually dominates, and one should expect the DD-enabled quantum speedup to have a finite-sized upper limit. The fact that this

upper limit is not observed in our experiments satisfies a key goal of implementing a quantum algorithm on a NISQ device, namely to check whether a quantum advantage is already accessible even before the advent of fault-tolerance, up to the largest problem sizes supported by the device. We have shown here that, with the help of error suppression via DD, this is indeed the case.

Another natural question is to what extent the speedup reported here can be further improved. We certainly expect that methods such as error mitigation [46] and further DD sequence optimization [31, 47–49] will have such an effect, though TTS_Q should then account for the additional classical computation time they incur. Device-tailored optimization of DD sequences with advanced low-level pulse control is an exciting frontier that remains largely unexplored and appears particularly promising. While we focused on superconducting-qubit devices, DD-protection can be beneficial across platforms, as all NISQ devices are affected by computational errors such as decoherence and crosstalk.

An ideal quantum computer would reduce the exponential growth of the classical TTS for the ssBV- n problem to a linear one. Our results are comparatively less impressive: we demonstrated what amounts to a polynomial quantum speedup, by reducing the exponent of the TTS scaling below its classical minimum. Our work provides a path to testing such speedups across platforms and algorithms in the NISQ era.

Methods

REDUCTION FROM SSBV- n TO SSBV- m

Since the oracle acts trivially on the i -th qubit if $b_i = 0$, the Hadamard gate pairs on the last $n - k$ qubits cancel. Therefore, the only difference between $b = 1^k 0^{n-k}$ and $b = 1^k 0^{m-k}$ is that the BV circuit for $|b| = n$ or $|b| = m$ applies *cancelling* Hadamard gates to the last $n - k$ or $m - k$ qubits, respectively. Now let $m \in [k, n - 1]$; then all the circuits for $b = 1^k 0^{m-k}$ in theory have the identical output as the circuit for $b = 1^k 0^{n-k}$, as illustrated in Fig. 5. We may thus extract the ssBV- m results from the ssBV- n results by running only the BV- n circuits and tracing over the last $n - m$ data qubits (see Appendix B for a detailed proof of this statement, including in the open system case), a practice we implemented in our experiments and subsequent analysis.

CIRCUIT DEPTH REDUCTION

A crucial ingredient in our implementation is a simple method for circuit depth reduction, needed to overcome the limited connectivity of the Montreal and Cairo chip architectures, where most qubits have only two neighbors, and some have three. This necessitates many SWAP operations in order to implement a CNOT between non-neighboring qubits, as required according to Fig. 1. While implementing a SWAP requires three CNOTs, by using the circuit identity $\text{CNOT}_{12} \text{SWAP}_{12} = \text{CNOT}_{21} \text{CNOT}_{12}$, we can implement a CNOT followed by a SWAP with just two CNOTs. On the heavy-hex layout of Montreal and Cairo, we found that

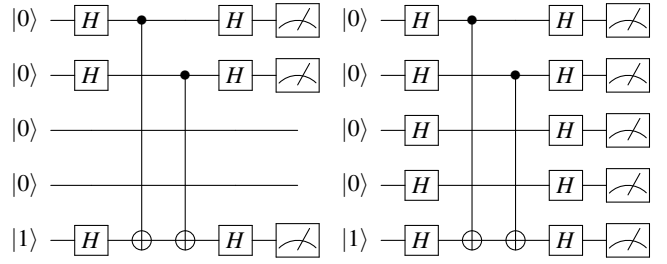


FIG. 5. Equivalent circuits used in our reduction from the circuit for $b = 1^k 0^{n-k}$ to the circuits for $b = 1^k 0^{m-k}$ with $m \in [k, n - 1]$. Illustrated on the left is BV-2 with the $b = 11$ oracle ($m = 2$ and $k = 2$), and on the right BV-4 with the $b = 1100$ oracle ($n = 4$ and $k = 2$). The left circuit is obtained from the right circuit by tracing over the last $n - k = 2$ data qubits.

the number of CNOTs required for implementing ssBV- n in this manner scales as $1.76n$. Our longest circuit, ssBV-26, required a total of 44 CNOTs, reduced from 80 CNOTs had we used the standard SWAP method. See Appendix D for more details.

DATA COLLECTION AND ERROR ANALYSIS

We implemented each unique circuit for 100,000 shots and 32,000 shots on Cairo and Montreal, respectively. We then sampled the corresponding results for all BV- n oracles using bootstrapping [50] and report the mean TTS for BV- n along with error bars corresponding to $\pm 5\sigma$ for the bootstrapped distribution (see Appendix E for more details).

COMPUTATION OF THE WORST-CASE TTS SCALING

To compute the scaling exponents reported in Fig. 3, we first fit $TTS \propto 2^{\lambda_{l,u} n}$ to the data for $n \in [l, u]$ with $l \in [1, u - 2]$ and $u \in [3, n'_{\max}]$, where n'_{\max} is the largest n for which we have TTS data, i.e., $n'_{\max} \in \{16, 20, 23, 26\}$ for {Montreal w/o DD, Cairo w/o DD, Cairo w/DD, Montreal w/DD}, respectively. In other words, $\lambda_{l, n'_{\max}}$ is the slope obtained by fitting to the data between l and n'_{\max} . We then obtain the asymptotic speedup exponent via $\lambda = \max_l \lambda_{l, n'_{\max}}$. By taking the max, we ensure that the speedup exponent thus estimated is conservative, i.e., represents the worst-case scaling compatible with the data. Similarly, Fig. 4 shows the speedup exponent $\lambda_{h_{\max}} = \max_l \lambda_{l, h_{\max}}$, i.e., the maximum local derivative of each of the curves in Fig. 3 for $n \leq h_{\max}$. All λ values are reported with a 2σ confidence interval obtained after bootstrapping. For complete details see Appendix E.

DD SEQUENCE PLACEMENT

The placement of DD sequences is determined by idle times (gaps) in the quantum circuit. These gaps arise because the algorithm specifies them or due to limited connectivity of the underlying architecture, which requires information swapping between some qubits while others are idle. Here we implemented one repetition of a pulse sequence that fits precisely in a gap, illustrated schematically in Fig. 1(bottom). Based on the results of the survey of DD sequences [51], we used the universally robust (UR $_n$ [38]) sequences UR $_{14}$ and UR $_{18}$ on

Montreal and Cairo, respectively. See Appendix F for details.

ACKNOWLEDGEMENTS

Access to the IBM Quantum Network was obtained through the membership of UNM in the IBM Quantum Hub at NC State. We are grateful to UNM for generously providing us access through their membership. This material is based in part upon work supported by the National Science Foundation the Quantum Leap Big Idea under Grant No. OMA-1936388. This work is also partially supported by a DOE/HEP QuantISED program grant, QCCFP/Quantum Machine Learning and Quantum Computation Frameworks (QCCFP-QMLQCF) for HEP, Grant No. DE-SC0019219. We are grateful to Dr. Namit Anand, Dr. Victor Kasatkin, and Dr. Evgeny Mozgunov for useful comments on the manuscript.

DATA AND CODE AVAILABILITY

The data supporting the findings of this paper are available at <https://tinyurl.com/ssBV-data>. The code used in this paper is available at github.com/USCqserver/bv-quantum-speedup.

Appendix A: Prior better-than-classical results

Quantum supremacy [52] has been demonstrated for efficiently sampling pseudo-random quantum circuits [11, 12] and boson sampling [13]. Assuming that it takes exponential time to solve an NP-complete problem, a quantum advantage in an interactive prover-verifier setting was demonstrated in Ref. [22]. These results all rely on various complexity-theoretic conjectures [14, 15, 53] to perform computational tasks that are beyond the capability of any classical computer. They are also susceptible to the boundaries defined by the capabilities of ever-improving classical supercomputers and algorithms [54].

Quantum annealing hardware based on superconducting flux qubits was used to demonstrate a speedup against simulated annealing for certain specially crafted spin-glass problems [55]. However, the speedup did not hold against other classical algorithms (such as quantum Monte Carlo). Another recent experiment used a variational quantum adiabatic algorithm, implemented using Rydberg atom arrays, to demonstrate a solution of the Maximum Independent Set problem with a quantum advantage as a function of problem hardness (not problem size) against simulated annealing [25]. The latter was constrained to the same effective circuit depth as the quantum implementation. The speedup was not tested against state-of-the-art classical algorithms, such as parallel tempering with iso-energetic cluster moves [56].

A quantum linear optics device solved the quantum coupon collection problem in fewer attempts than a classical strategy [24]. Likewise, using a nanophotonic device, a quantum speedup in learning time was demonstrated in a reinforcement learning setup [21]. However, these demonstrations do not

scale: in both cases the authors show that it is optimal to revert to the classical strategy even for the cases they tested, when the problem sizes or learning times increase beyond a certain threshold.

Recent work used hybrid quantum-classical learning with quantum-enhanced experiments to demonstrate an experimental quantum advantage [20]. This work proves an exponential quantum-classical separation in terms of the number of experiments required to achieve a given accuracy in the machine learning task, and demonstrates this separation experimentally. In a similar vein, a quantum advantage was demonstrated in a setting of supervised learning assisted by an entangled sensor network against classical support vector machines (an entanglement-enabled reduction in the error probability for classification of multidimensional radio-frequency signals) [23]. The most important difference is that in both cases this involving quantum data (i.e., learning on quantum states), whereas in our case the problem being solved is classical: winning a guessing game involving purely classical data (secret bitstrings). Another important difference between these results and ours is that the former are hybrid quantum-classical approaches, whereas we are considering the scaling of a purely quantum algorithm. The difference is significant in that in the former case the cost of the classical processing (such as variational optimization) is not fully accounted for. We do not expect this cost to change an exponential separation, but this point makes a direct comparison with our result slightly more challenging.

Some of our results are directly comparable to various NISQ implementations of oracular quantum algorithms. Ref. [18] implemented the BV and Hidden Shift (HS) algorithms for $n = 10$ on an 11-qubit trapped-ion device, which was the largest and most successful implementation of these algorithms at the time (later superseded by BV-11 and BV-20 on superconducting and trapped-ion devices respectively [44]). Moreover, they demonstrated better-than-classical performance on both algorithms, by crossing the BQP threshold for BV and by finding higher-than-classical success probabilities for HS, at the fixed problem size of $n = 10$. Likewise, Refs [17] and [19] respectively used 3-qubit trapped-ion and trimon devices to implement oracular algorithms, and 4-qubit and 5-qubit versions of Grover’s algorithm were implemented on various IBMQ devices [57]. In all these cases claims of better-than-classical results focus on crossing a classical success probability threshold at a fixed problem size such that $p_{\text{quantum}} > p_{\text{classical}}$. However, this argument is insufficient for establishing a quantum speedup, which must be based on the scaling with n of a time-based metric such as the TTS [6] or related metrics [58–60].

Appendix B: Reduction from ssBV- n to ssBV- n for CPTP maps

We extracted the ssBV- m results (for $m < n$) from the ssBV- n results by tracing over the last $n - m$ qubits. Here we prove the equivalence of our procedure to actually running the ssBV- m circuits, as long as the completely positive, trace preserving (CPTP) map governing the circuit in the open system case fac-

tors into a product over the ‘‘marked’’ and ‘‘unmarked’’ qubits, i.e., those corresponding to a 1 (marked) or 0 (unmarked) in the bitstring b that defines the given oracle.

We first consider the ideal ssBV- n algorithm without any open-system effects. The initial state is $|\psi_0\rangle = |0\rangle^{\otimes n} \otimes |1\rangle$. Applying the initial Hadamard layer yields

$$|\psi_1\rangle = (H^{\otimes n+1})|\psi_0\rangle = |+\rangle^{\otimes n} \otimes |-\rangle. \quad (\text{B1})$$

We then apply the oracle corresponding to the hidden bitstring $b \in \{0, 1\}^n$, i.e., $O_{f_b}|x\rangle|y\rangle = |x\rangle|y \oplus f_b(x)\rangle$, so that the state becomes

$$|\psi_2\rangle = O_{f_b}|\psi_1\rangle = \quad (\text{B2a})$$

$$= O_{f_b} \left[\frac{1}{\sqrt{2^{n+1}}} \sum_{x \in \{0,1\}^n} |x\rangle(|0\rangle - |1\rangle) \right] \quad (\text{B2b})$$

$$= \frac{1}{\sqrt{2^{n+1}}} \sum_{x \in \{0,1\}^n} |x\rangle(|f_b(x)\rangle - |1 \oplus f_b(x)\rangle) \quad (\text{B2c})$$

$$= \frac{1}{\sqrt{2^n}} \sum_x (-1)^{f_b(x)} |x\rangle|-\rangle. \quad (\text{B2d})$$

In the last line above, we use the fact that for any x , $f_b(x)$ is either 0 or 1, i.e.,

$$|x\rangle(|f_b(x)\rangle - |1 \oplus f_b(x)\rangle) = \begin{cases} |x\rangle(|0\rangle - |1\rangle) & f_b(x) = 0 \\ |x\rangle(|1\rangle - |0\rangle) & f_b(x) = 1 \end{cases} \quad (\text{B3a})$$

$$= (-1)^{f_b(x)} |x\rangle(|0\rangle - |1\rangle). \quad (\text{B3b})$$

The final Hadamard layer is applied next, and, using $f_b(x) = b \cdot x \pmod 2$:

$$|\psi_3\rangle = H^{\otimes n+1}|\psi_2\rangle \quad (\text{B4a})$$

$$= \left(H^{\otimes n} \frac{1}{\sqrt{2^n}} \sum_x (-1)^{b \cdot x} |x\rangle \right) \otimes H|-\rangle = |b\rangle|1\rangle. \quad (\text{B4b})$$

In preparation of our more general discussion below, let us equivalently represent the action of ssBV- n with hidden bitstring b on some initial state ρ of the n data qubits and the ancilla qubit as

$$\text{BV}_n(b)[\rho] = \text{Tr}_{n+1} \left[\left(H^{\otimes n+1} \circ O_{f_b} \circ H^{\otimes n+1} \right) [\rho] \right], \quad (\text{B5})$$

where O_{f_b} represents the BV oracle, and Tr_{n+1} means that the state of the ancilla qubit (numbered $n+1$) is discarded at the end, so that $\text{BV}_n(b)[\rho]$ is the state of the n data qubits at the end of one run of the algorithm. Thus, if we write $\Pi_b = |b\rangle\langle b|$ and $|\psi_0\rangle\langle\psi_0| = \Pi_{0^n} \otimes \Pi_1$, then it follows from Eq. (B4) that $\text{BV}_n(b)[|\psi_0\rangle\langle\psi_0|] = \Pi_b$. In the main text and Methods we argued that if $b_n = 1^k 0^{n-k}$, then

$$\text{BV}_m(b_m)[\Pi_{0^m} \otimes \Pi_1] = \text{Tr}_{\{m+1, m+2, \dots, n\}} [\text{BV}_n(b_n)[\Pi_{0^n} \otimes \Pi_1]], \quad (\text{B6})$$

where the trace means that the states of qubits $\{m+1, m+2, \dots, n\}$ are discarded from the result of running $\text{BV}_n(b_n)$.

To prove this claim in the absence of any noise, note that:

$$\text{Tr}_{\{m+1, m+2, \dots, n\}} [\text{BV}_n(b_n)[|\psi_0\rangle\langle\psi_0|]] \quad (\text{B7a})$$

$$= \text{Tr}_{\{m+1, m+2, \dots, n\}} [\Pi_{b_n}] \quad (\text{B7b})$$

$$= \text{Tr}_{\{m+1, m+2, \dots, n\}} [\Pi_{1^k 0^{n-k}}] \quad (\text{B7c})$$

$$= \text{Tr}_{\{m+1, m+2, \dots, n\}} [\Pi_{1^k 0^{n-k}} \otimes \Pi_{0^{n-m}}] \quad (\text{B7d})$$

$$= \Pi_{1^k 0^{n-k}} \quad (\text{B7e})$$

$$= \text{BV}_m(b_m)[\Pi_{0^m} \otimes \Pi_1], \quad (\text{B7f})$$

as claimed.

Now consider the case where each gate is represented not by a unitary but a CPTP map. For convenience, let us renumber the ancilla to be the 0th qubit instead of the $n+1$ th qubit. We can rewrite the initial state as

$$|\psi_0\rangle\langle\psi_0| = \Pi_1 \otimes \Pi_{0^n} = \rho_A \otimes \rho_B, \quad (\text{B8})$$

where $\rho_A = (\Pi_1 \otimes \Pi_{0^m})$ and $\rho_B = \Pi_{0^{n-m}}$. The BV oracle does not introduce any two-qubit gates between qubit sectors $A = \{0, 1, \dots, m\}$ and $B = \{m+1, m+2, \dots, n\}$, so it is reasonable to assume that under the coupling to the environment they remain uncoupled (as long as there is no unintended crosstalk between the two sectors). Therefore, the CPTP map for the noisy ssBV- n algorithm will be

$$\mathcal{BV}_n(b_n)[\rho_A \otimes \rho_B] = \text{Tr}_0 \left[(\mathcal{H}_A \otimes \mathcal{H}_B) \circ (\mathcal{O}_A \otimes \mathcal{O}_B) \circ (\mathcal{H}_A \otimes \mathcal{H}_B) [\rho_A \otimes \rho_B] \right], \quad (\text{B9})$$

where $\mathcal{H}_{A,B}$ and $\mathcal{O}_{A,B}$ represent the CPTP maps corresponding to the experimental implementation of the unitaries H (multi-qubit Hadamard) and O (oracle) acting on qubit sectors A, B . Recall that for arbitrary CPTP maps \mathcal{U} and \mathcal{V} acting on a tensor-product space

$$\mathcal{U} \otimes \mathcal{V} [\rho \otimes \sigma] = \mathcal{U}[\rho] \otimes \mathcal{V}[\sigma]. \quad (\text{B10})$$

Therefore,

$$\text{Tr}_{\{B\}} [\mathcal{BV}_n(b_n)[|\psi_0\rangle\langle\psi_0|]] \quad (\text{B11a})$$

$$= \text{Tr}_{\{0,B\}} \left[(\mathcal{H}_A \otimes \mathcal{H}_B) \circ (\mathcal{O}_A \otimes \mathcal{O}_B) \circ (\mathcal{H}_A \otimes \mathcal{H}_B) [\rho_A \otimes \rho_B] \right] \quad (\text{B11b})$$

$$= \text{Tr}_{\{0,B\}} \left[(\mathcal{H}_A \circ \mathcal{O}_A \circ \mathcal{H}_A) [\rho_A] \otimes (\mathcal{H}_B \circ \mathcal{O}_B \circ \mathcal{H}_B) [\rho_B] \right] \quad (\text{B11c})$$

$$= \text{Tr}_{\{0\}} \left[(\mathcal{H}_A \circ \mathcal{O}_A \circ \mathcal{H}_A) [\rho_A] \right] \quad (\text{B11d})$$

$$= \mathcal{BV}_m(b_m)[\rho_A] \quad (\text{B11e})$$

$$= \mathcal{BV}_m(b_m)[\Pi_1 \otimes \Pi_{0^m}]. \quad (\text{B11f})$$

This is the CPTP map generalization of the closed-system result Eq. (B6), and it shows that the reduction from ssBV- n to ssBV- m holds rigorously also in the open system setting, as long as the CPTP map factors according to the qubit sectors A and B .

Ref. [29] considered in detail how the state of the spectator qubits can change the effect of crosstalk on neighboring qubits. In particular, it showed that while crosstalk can be exacerbated if the spectator qubits are in a superposition state

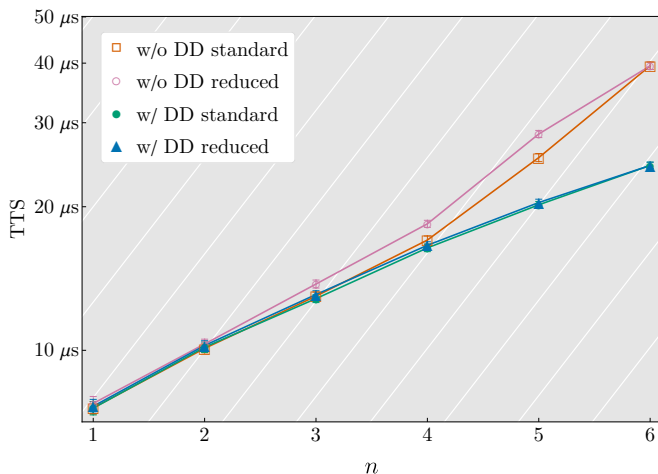


FIG. 6. Comparison of the effect of crosstalk without and with DD (the UR_{14} sequence). $TTS(n)$ is shown for `ibmq_jakarta`. While $TTS_{\text{standard}} \leq TTS_{\text{reduced}}$ without DD protection, the TTS results are statistically indistinguishable in the presence of DD.

(as is the case here), this effect can be counteracted by using DD. The improvement we have reported under DD further confirms this observation in the context of $ssBV-n$ circuits.

To investigate this more closely, we implemented $ssBV-n$ for $n = 1$ to 6 on the 7-qubit `ibmq_jakarta` processor, and considered both the standard and the reduced setup (i.e., both sides of Fig. 5). The TTS results are shown in Fig. 6. Without DD, we expect cross-talk to introduce unwanted coupling between the marked and unmarked qubits, which lowers the success probability and hence increases the TTS. This is what we already observed on Montreal and Cairo, and is also seen on Jakarta. Furthermore, we expect the proof of the reduction from $ssBV-n$ to $ssBV-m$ to break down in the presence of cross-talk, and indeed, we observe in Fig. 6 that $TTS_{\text{standard}} \neq TTS_{\text{reduced}}$ without DD-protection. However, with DD the TTS is statistically identical for both setups. This further validates our use of the reduced setup.

Appendix C: Device Specifications

Both Montreal and Cairo are 27-qubit devices with a connectivity architecture as shown in Fig. 7. They have quantum volumes of 128 and 64 and are built using the IBM Quantum Falcon r4 and r5.11 processors, respectively [40]. Single qubit gates are performed by driving a DRAG pulse, and two-qubit gates are echoed cross-resonance (CR) gates. T_1 , T_2 times, and gate as well as measurement errors and durations are detailed in Table I.

Recall that in the main text we modeled the hypothetical, ideal $TTS_Q(n)$ as $c\tau_{2q}n + \tau_0$. This linear model is actually a slight oversimplification; the ideal TTS (assuming no decoherence) for Montreal and Cairo as a function of n is shown in Fig. 8, and only becomes linear for $n > 2$ (Montreal) or $n > 5$ (Cairo). The dashed lines shown in Fig. 3 are identical to the data shown in Fig. 8 (not the linear fits). As both

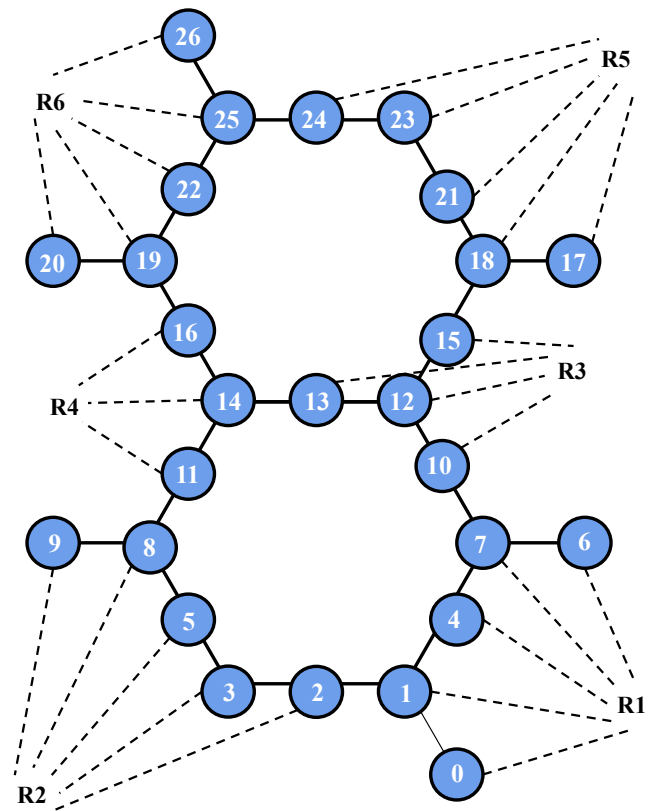


FIG. 7. Schematic of the lattice connectivity for 27-qubit devices with the heavy-hex layout [30]. The dashed lines connect qubits that are multiplexed together for readout.

	Montreal			Cairo		
	Min	Mean	Max	Min	Mean	Max
T_1 (μs)	57.57	113.2	187.1	39.93	102.19	198.93
T_2 (μs)	22.58	99.72	198.71	18.58	114.19	290.06
1QG Error (%)	0.02	0.04	0.15	0.01	0.03	0.07
2QG Error (%)	0.57	1.35	6.09	0.52	4.64	100.0
1QG Duration (μs)	0.04	0.04	0.04	0.02	0.02	0.02
2QG Duration (μs)	0.27	0.43	0.63	0.16	0.31	0.71
RO Error (%)	0.79	2.59	10.66	0.47	1.39	4.89
RO Duration (μs)	5.2	5.2	5.2	0.73	0.73	0.73

TABLE I. Device specifications for Montreal and Cairo on March 12, 2022. 1QG and 2QG denote 1-qubit gate and 2-qubit gate, respectively. RO denotes readout.

readout and 2-qubit gate durations are higher for Montreal, $TTS_{\text{Montreal}} > TTS_{\text{Cairo}}$. The TTS growth rates (for $n > 5$) are $c\tau_{2q} = 0.40\mu\text{s}$ and $c\tau_{2q} = 0.27\mu\text{s}$, and are slightly lower than the average 2-qubit gate durations of $0.43\mu\text{s}$ and $0.31\mu\text{s}$ for Montreal and Cairo, respectively. The intercepts are at $5.28\mu\text{s}$ and $0.77\mu\text{s}$ for Montreal and Cairo, respectively.

We used the entire chip for Montreal, but Cairo had three noisy qubits that were left out from the experiments reported in Fig. 3. To explain this, Fig. 9 shows our $ssBV-n$ results on the entire Cairo chip using a different logical-to-physical implementation than Fig. 3. Here, the largest problem sizes

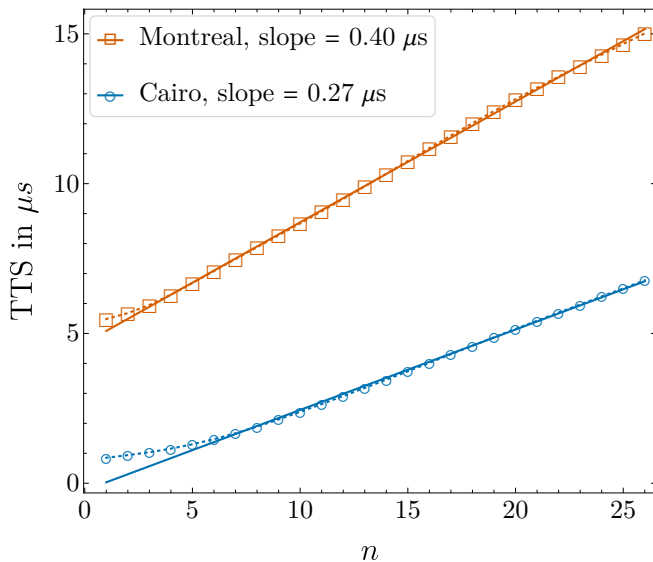


FIG. 8. The hypothetical, ideal TTS for Montreal and Cairo as a function of n . A deviation from linear scaling is seen for small n .

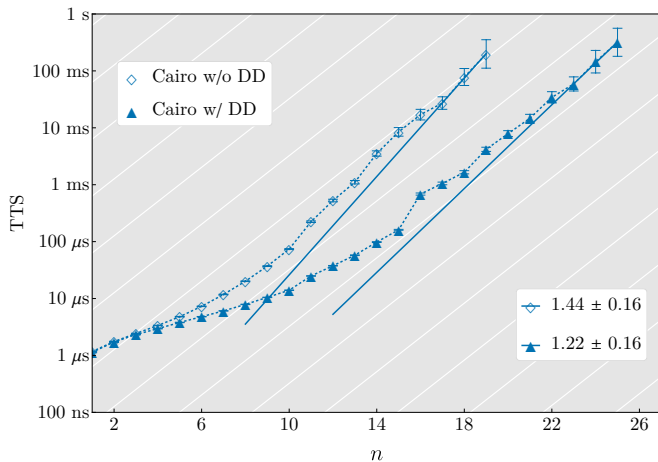


FIG. 9. Results from Cairo with a different logical to physical qubit mapping than used in Fig. 3, using all 27 qubits. These runs were performed on January 2nd, 2022. Due to a significant readout error in Q19, there is an abrupt jump in the TTS at $n = 15$. Consequently, qubits Q19, Q20, and Q22 were left out of all subsequent experiments.

solved with and without DD are $n = 19$ and 25 respectively. There is an abrupt jump in the TTS at $n = 15$ due to a large readout error in Q19. In particular, the readout error for Q19 is 12.9%, which is an order of magnitude higher than the average readout error of 1.76%. Consequently, we used a different logical-to-physical embedding where the three faulty qubits, Q19 and its neighbors Q20 and Q22 (see Fig. 7), were left out of the experiment. While this reduced the largest problem size we could solve in the DD setting (from $n = 26$ to $n = 23$), it allowed us to extract λ without being affected by the anomalous readout error in Q19. Overall, we effectively treated Cairo as a 24-qubit device in all our subsequent experiments.

Appendix D: Reduction of circuit depth: CNOT-efficient SWAPs for ssBV- n

A fully connected architecture would allow BV- n to be implemented with n two-qubit gates. Both Cairo and Montreal have a maximum connectivity of 3, and most qubits are connected to 2 others; see Fig. 7. Generally, circuit transpilers deal with the sparseness by swapping qubits as necessary. The BV algorithms requires us to entangle the “marked” qubits (those corresponding to a 1 in the bitstring b that defines the given oracle) with the ancilla, and so we must swap the unmarked qubits when the ancilla and the marked qubit are not directly coupled. This is equivalent to swapping the ancilla instead of the marked qubit. While implementing a SWAP requires three CNOTs, by using the circuit identity $\text{CNOT}_{12} \text{SWAP}_{12} = \text{CNOT}_{21} \text{CNOT}_{12}$, we can implement a CNOT followed by a SWAP with just two CNOTs. Fig. 10 illustrates this for the ssBV-2 case. Overall, swapping the ancilla reduces the CNOT scaling from $4n$ to $2n$ for a linear architecture. On the heavy-hex layout, the number of CNOTs required for implementing ssBV- n is found to scale as $1.76n$, as shown in Fig. 11. For ssBV-26, our longest circuit, we used 44 CNOTs. This is because on top of the 26 CNOTs between the marked and the ancilla qubit, 18 CNOTs were needed to perform the SWAP. If each of the 18 SWAPs required 3 extra CNOTs instead, then ssBV-26 would require 80 CNOTs.

Appendix E: Bootstrapping

In all our TTS figures, we report $\text{TTS}_{\text{avg}} \equiv \text{mean}_i(\text{TTS}_i)$, where TTS_i is the time-to-solution for the i 'th oracle. Each oracular experiment was repeated for 32,000 (100,000) shots on Montreal (Cairo), and we counted how many of these experiments returned the correct answer. We bootstrapped over the observed counts, using the method described in [50], to get 100 sampled versions of each oracular experiment. The reported TTS values and the error bars correspond, respectively, to the expected value and $\pm 5\sigma$ for TTS_{avg} computed from these bootstrapped samples. It is possible for the success probability for a given oracle to be non-zero and yet for some of the bootstrapped samples to have no successful counts. In such cases, we discarded those bootstrapped samples as this would lead to infinite TTS. An actual infinite TTS means that the solution was not observed during any repetition of the experiment, i.e., $p_s = 0$.

To obtain the confidence intervals for the speedup exponents λ , we first use Mathematica's LinearModelFit function to compute the worst-case fit on each bootstrapped sample. We then report the expected value with 2σ confidence intervals obtained from the ensemble of λ s.

Appendix F: Dynamical decoupling details

We tested a large set of known DD pulse sequences on the BV-10 oracle $b = 1^{10}$ and then considered the performance of

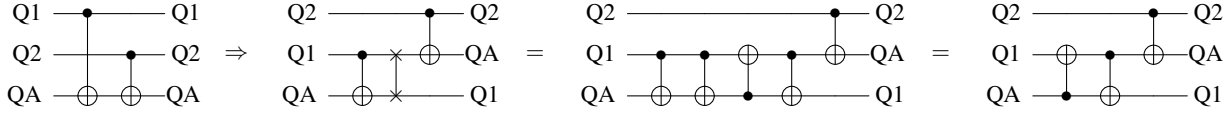


FIG. 10. Example of an ssBV implementation using ancilla swapping. Here we consider the circuit for implementing the oracle with $b = 11$ for ssBV-2 on a linear architecture with qubit connectivity Q2-Q1-QA (left). The standard swapping technique (second from left) requires 5 CNOTs (second from right), but choosing to swap the ancilla allows the circuit to be implemented with just 3 CNOTs (right).

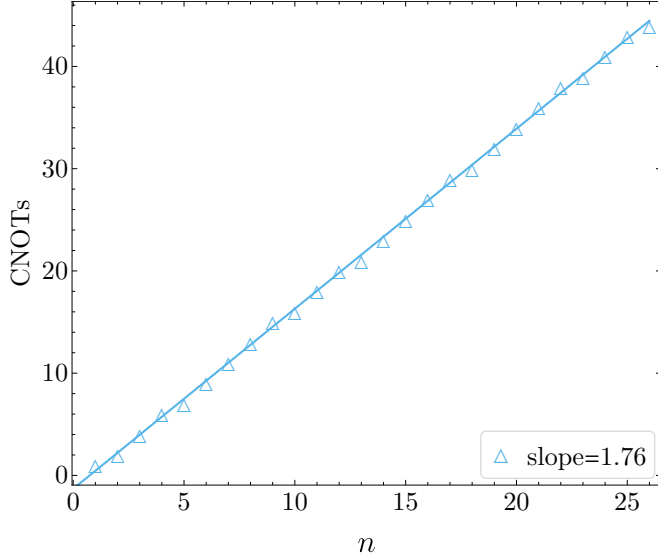


FIG. 11. The number of CNOTs used to implement the $b = 1^n$ oracle is shown as a function of n . This number would scale as $2n$ for a chain, but for the heavy-hex architecture, it scales as $1.76n$. As both Montreal and Cairo use the same architecture, this number is same for both.

the top four sequences we identified in this manner on the entire ssBV- n experiment (not shown). All such DD sequences outperformed the unprotected implementation on both Montreal and Cairo, and the specific choice of the DD sequence had little impact on the speedup exponents λ . The results shown in the main text utilize the universally robust (UR $_n$) sequences [38], which are known to perform well on superconducting devices [28, 37, 39].

The UR $_n$ sequence for $n \geq 4$ and n even is defined as

$$\text{UR}_n = (\pi)_{\phi_1} - (\pi)_{\phi_2} - \dots - (\pi)_{\phi_n} \quad (\text{F1a})$$

$$\phi_k = \frac{(k-1)(k-2)}{2} \Phi^{(n)} + (k-1)\phi_2 \quad (\text{F1b})$$

$$\Phi^{(4m)} = \frac{\pi}{m} \quad \Phi^{(4m+2)} = \frac{2m\pi}{2m+1}, \quad (\text{F1c})$$

where $(\pi)_{\phi}$ is a π rotation about an axis which makes an angle ϕ with the x -axis, and where ϕ_1 is a free parameter usually set to 0 by convention, and $\phi_2 = \pi/2$ is a standard choice we used. This is done so that UR $_4 = \text{XY4}$, the well-known universal DD sequence [61], as discussed in Ref. [38].

We implemented one repetition of the DD sequence in all available idle time gaps (see Fig. 1) and did not attempt to optimize the pulse shape or pulse placement. Such an optimization would undoubtedly further improve performance, and presents a fruitful future research direction; see, e.g., Refs. [29, 47, 48].

-
- [1] Deutsch, D. & Jozsa, R. Rapid solution of problems by quantum computation. *Proc. R. Soc. Lond. A* **439**, 553–558 (1992). URL <https://doi.org/10.1098/rspa.1992.0167>.
- [2] Bernstein, E. & Vazirani, U. Quantum Complexity Theory. *SIAM J. Comput.* **26**, 1411–1473 (1997). URL <https://doi.org/10.1137/S0097539796300921>.
- [3] Grover, L. K. A fast quantum mechanical algorithm for database search. In *Proceedings of the Twenty-Eighth Annual ACM Symposium on Theory of Computing*, 212–219 (Association for Computing Machinery, Philadelphia, Pennsylvania, USA, 1996).
- [4] Shor, P. W. Polynomial-time algorithms for prime factorization and discrete logarithms on a quantum computer. *SIAM Review* **41**, 303–332 (1999). URL <https://epubs.siam.org/doi/abs/10.1137/S0036144598347011>.
- [5] Montanaro, A. Quantum algorithms: An overview. *NPJ Quantum Inf.* **2**, 15023 (2016). URL <https://www.nature.com/articles/npjqi201523>.
- [6] Rønnow, T. F. *et al.* Defining and detecting quantum speedup. *Science* **345**, 420–424 (2014). URL <https://doi.org/10.1126/science.1252319>.
- [7] Preskill, J. Quantum computing in the nisq era and beyond. *Quantum* **2**, 79 (2018). URL <http://dx.doi.org/10.22331/q-2018-08-06-79>.
- [8] IBM Quantum. URL <https://quantum-computing.ibm.com/>.
- [9] Viola, L. & Lloyd, S. Dynamical suppression of decoherence in two-state quantum systems. *Phys. Rev. A* **58**, 2733–2744 (1998). URL <https://link.aps.org/doi/10.1103/PhysRevA.58.2733>.
- [10] Suter, D. & Álvarez, G. A. Colloquium: Protecting quantum information against environmental noise. *Rev. Mod. Phys.* **88**, 041001– (2016). URL <https://link.aps.org/doi/10.1103/RevModPhys.88.041001>.
- [11] Arute, F. *et al.* Quantum supremacy using a programmable superconducting processor. *Nature* **574**, 505–510 (2019). URL

- <https://doi.org/10.1038/s41586-019-1666-5>.
- [12] Wu, Y. *et al.* Strong quantum computational advantage using a superconducting quantum processor. *Phys. Rev. Lett.* **127**, 180501– (2021). URL <https://link.aps.org/doi/10.1103/PhysRevLett.127.180501>.
- [13] Zhong, H.-S. *et al.* Phase-programmable gaussian boson sampling using stimulated squeezed light. *Phys. Rev. Lett.* **127**, 180502– (2021). URL <https://link.aps.org/doi/10.1103/PhysRevLett.127.180502>.
- [14] Aaronson, S. & Chen, L. Complexity-Theoretic Foundations of Quantum Supremacy Experiments. In O’Donnell, R. (ed.) *32nd Computational Complexity Conference (CCC 2017)*, vol. 79 of *Leibniz International Proceedings in Informatics (LIPIcs)*, 22:1–22:67 (Schloss Dagstuhl–Leibniz-Zentrum fuer Informatik, Dagstuhl, Germany, 2017). URL <http://drops.dagstuhl.de/opus/volltexte/2017/7527>.
- [15] Harrow, A. W. & Montanaro, A. Quantum computational supremacy. *Nature* **549**, 203 EP – (2017). URL <http://dx.doi.org/10.1038/nature23458>.
- [16] Hangleiter, D. & Eisert, J. Computational advantage of quantum random sampling (2022). URL <https://arxiv.org/abs/2206.04079>. 2206.04079.
- [17] Figgatt, C. *et al.* Complete 3-Qubit Grover search on a programmable quantum computer. *Nat. Commun.* **8**, 1–9 (2017). URL <https://www.nature.com/articles/s41467-017-01904-7>.
- [18] Wright, K. *et al.* Benchmarking an 11-qubit quantum computer. *Nat. Commun.* **10**, 5464 (2019). URL <https://www.nature.com/articles/s41467-019-13534-2>.
- [19] Roy, T. *et al.* Programmable Superconducting Processor with Native Three-Qubit Gates. *Phys. Rev. Applied* **14**, 014072 (2020). URL <https://journals.aps.org/prapplied/abstract/10.1103/PhysRevApplied.14.014072>.
- [20] Huang, H.-Y. *et al.* Quantum advantage in learning from experiments (2021). URL <https://arxiv.org/abs/2112.00778>.
- [21] Saggio, V. *et al.* Experimental quantum speed-up in reinforcement learning agents. *Nature* **591**, 229–233 (2021). URL <https://doi.org/10.1038/s41586-021-03242-7>.
- [22] Centrone, F., Kumar, N., Diamanti, E. & Kerenidis, I. Experimental demonstration of quantum advantage for NP verification with limited information. *Nat. Commun.* **12**, 850 (2021). URL <https://www.nature.com/articles/s41467-021-21119-1>.
- [23] Xia, Y., Li, W., Zhuang, Q. & Zhang, Z. Quantum-Enhanced Data Classification with a Variational Entangled Sensor Network. *Phys. Rev. X* **11**, 021047 (2021). URL <https://journals.aps.org/prx/abstract/10.1103/PhysRevX.11.021047>.
- [24] Zhou, M.-G. *et al.* Experimental quantum advantage with quantum coupon collector. *Research* **2022** (2022). URL <https://doi.org/10.34133/2022/9798679>.
- [25] Ebadi, S. *et al.* Quantum optimization of maximum independent set using rydberg atom arrays. *Science* **376**, 1209–1215 (2022). URL <https://doi.org/10.1126/science.abo6587>.
- [26] Bravyi, S. & Gosset, D. Improved classical simulation of quantum circuits dominated by clifford gates. *Phys. Rev. Lett.* **116**, 250501– (2016). URL <https://link.aps.org/doi/10.1103/PhysRevLett.116.250501>.
- [27] Pokharel, B., Anand, N., Fortman, B. & Lidar, D. A. Demonstration of fidelity improvement using dynamical decoupling with superconducting qubits. *Phys. Rev. Lett.* **121**, 220502 (2018). URL <https://link.aps.org/doi/10.1103/PhysRevLett.121.220502>.
- [28] Souza, A. M. Process tomography of robust dynamical decoupling in superconducting qubits (2020). URL <https://arxiv.org/abs/2006.10585>. 2006.10585.
- [29] Tripathi, V. *et al.* Suppression of crosstalk in superconducting qubits using dynamical decoupling (2021). URL <https://arxiv.org/abs/2108.04530>. 2108.04530.
- [30] Jurcevic, P. *et al.* Demonstration of quantum volume 64 on a superconducting quantum computing system. *Quantum Sci. Technol.* **6**, 025020 (2021). URL <https://iopscience.iop.org/article/10.1088/2058-9565/abe519>.
- [31] Ravi, G. S. *et al.* VAQEM: A Variational Approach to Quantum Error Mitigation (2021). URL <https://arxiv.org/abs/2112.05821>. 2112.05821.
- [32] Viola, L., Lloyd, S. & Knill, E. Universal control of decoupled quantum systems. *Phys. Rev. Lett.* **83**, 4888–4891 (1999). URL <http://link.aps.org/doi/10.1103/PhysRevLett.83.4888>.
- [33] Khodjasteh, K. & Lidar, D. A. Rigorous bounds on the performance of a hybrid dynamical-decoupling quantum-computing scheme. *Phys. Rev. A* **78**, 012355– (2008). URL <https://link.aps.org/doi/10.1103/PhysRevA.78.012355>.
- [34] Khodjasteh, K. & Viola, L. Dynamically error-corrected gates for universal quantum computation. *Phys. Rev. Lett.* **102**, 080501– (2009). URL <https://link.aps.org/doi/10.1103/PhysRevLett.102.080501>.
- [35] West, J. R., Lidar, D. A., Fong, B. H. & Gyure, M. F. High fidelity quantum gates via dynamical decoupling. *Phys. Rev. Lett.* **105**, 230503 (2010). URL <http://dx.doi.org/10.1103/PhysRevLett.105.230503>.
- [36] Ng, H. K., Lidar, D. A. & Preskill, J. Combining dynamical decoupling with fault-tolerant quantum computation. *Phys. Rev. A* **84**, 012305– (2011). URL <http://link.aps.org/doi/10.1103/PhysRevA.84.012305>.
- [37] Ezzell, N., Tewala, L., Pokharel, B., Quiroz, G. & Lidar, D. A. to be published (2022).
- [38] Genov, G. T., Schraft, D., Vitanov, N. V. & Halfmann, T. Arbitrarily accurate pulse sequences for robust dynamical decoupling. *Phys. Rev. Lett.* **118**, 133202– (2017). URL <https://link.aps.org/doi/10.1103/PhysRevLett.118.133202>.
- [39] Gautam, A., Arvind & Dorai, K. Protection of noisy multipartite entangled states of superconducting qubits via universally robust dynamical decoupling schemes (2021). URL <https://arxiv.org/abs/2112.10417>. 2112.05821.
- [40] Pelofske, E., Bäertschi, A. & Eidenbenz, S. Quantum Volume in Practice: What Users Can Expect from NISQ Devices (2022). URL <https://arxiv.org/abs/2203.03816>. 2112.05821.
- [41] Debnath, S. *et al.* Demonstration of a small programmable quantum computer with atomic qubits. *Nature* **536**, 63–66 (2016). URL <https://doi.org/10.1038/nature18648>.
- [42] Linke, N. M. *et al.* Experimental comparison of two quantum computing architectures. *Proc. Natl. Acad. Sci.* **114**, 3305–3310 (2017). URL <https://www.pnas.org/doi/full/10.1073/pnas.1618020114>.
- [43] Murali, P. *et al.* Full-stack, real-system quantum computer studies: Architectural comparisons and design insights. In *Proceedings of the 46th International Symposium on Computer Architecture*, 527–540 (Association for Computing Machinery, Phoenix, Arizona, 2019). URL <https://doi.org/10.1145/3307650.3322273>.
- [44] Lubinski, T. *et al.* Application-Oriented Performance Benchmarks for Quantum Computing (2021). URL <https://arxiv.org/abs/2110.03137>. 2110.03137.
- [45] Campbell, E. T., Terhal, B. M. & Vuillot, C. Roads towards fault-tolerant universal quantum computation. *Nature*

- 549, 172 EP – (2017). URL <http://dx.doi.org/10.1038/nature23460>.
- [46] Temme, K., Bravyi, S. & Gambetta, J. M. Error mitigation for short-depth quantum circuits. *Phys. Rev. Lett.* **119**, 180509– (2017). URL <https://link.aps.org/doi/10.1103/PhysRevLett.119.180509>.
- [47] Zlokapa, A. & Gheorghiu, A. A deep learning model for noise prediction on near-term quantum devices (2020). URL <https://arxiv.org/abs/2005.10811>. 2005.10811.
- [48] Das, P., Tannu, S., Dangwal, S. & Qureshi, M. Adapt: Mitigating idling errors in qubits via adaptive dynamical decoupling. In *MICRO-54: 54th Annual IEEE/ACM International Symposium on Microarchitecture*, 950–962 (ACM, Virtual Event Greece, 2021). URL <https://doi.org/10.1145/3466752.3480059>.
- [49] Niu, S. & Todri-Sanial, A. Analyzing Strategies for Dynamical Decoupling Insertion on IBM Quantum Computer (2022). URL <https://arxiv.org/abs/2204.14251>. 2204.14251.
- [50] Efron, B. Bootstrap Methods: Another Look at the Jackknife. In *Breakthroughs in Statistics: Methodology and Distribution*, 569–593 (Springer, New York, NY, 1992). URL https://doi.org/10.1007/978-1-4612-4380-9_41.
- [51] Ezzell, N., Pokharel, B., Tewala, L., Quiroz, G. & Lidar, D. A. Dynamical decoupling for superconducting qubits: a performance survey (2022). URL <https://arxiv.org/abs/2207.03670>. 2207.03670.
- [52] Preskill, J. Quantum computing and the entanglement frontier (2012). URL <http://arXiv.org/abs/1203.5813>. 1203.5813.
- [53] Lund, A. P., Bremner, M. J. & Ralph, T. C. Quantum sampling problems, bosonsampling and quantum supremacy. *NPJ Quantum Inf.* **3**, 15 (2017). URL <https://doi.org/10.1038/s41534-017-0018-2>.
- [54] Zlokapa, A., Boixo, S. & Lidar, D. Boundaries of quantum supremacy via random circuit sampling (2020). URL <https://arxiv.org/abs/2005.02464>. 2005.02464.
- [55] Albash, T. & Lidar, D. A. Demonstration of a scaling advantage for a quantum annealer over simulated annealing. *Phys. Rev. X* **8**, 031016– (2018). URL <https://link.aps.org/doi/10.1103/PhysRevX.8.031016>.
- [56] Zhu, Z., Ochoa, A. J. & Katzgraber, H. G. Efficient cluster algorithm for spin glasses in any space dimension. *Phys. Rev. Lett.* **115**, 077201 (2015). URL <http://link.aps.org/doi/10.1103/PhysRevLett.115.077201>.
- [57] Zhang, K., Rao, P., Yu, K., Lim, H. & Korepin, V. Implementation of efficient quantum search algorithms on NISQ computers. *Quant. Inf. Proc.* **20**, 233 (2021). URL <https://doi.org/10.1007%2Fs11128-021-03165-2>.
- [58] King, J., Yarkoni, S., Nevisi, M. M., Hilton, J. P. & McGeoch, C. C. Benchmarking a quantum annealing processor with the time-to-target metric (2015). URL <http://arXiv.org/abs/1508.05087>. 1508.05087.
- [59] Vinci, W. & Lidar, D. A. Optimally stopped optimization. *Phys. Rev. Applied* **6**, 054016– (2016). URL <http://link.aps.org/doi/10.1103/PhysRevApplied.6.054016>.
- [60] Mandrà, S., Zhu, Z., Wang, W., Perdomo-Ortiz, A. & Katzgraber, H. G. Strengths and weaknesses of weak-strong cluster problems: A detailed overview of state-of-the-art classical heuristics versus quantum approaches. *Phys. Rev. A* **94**, 022337– (2016). URL <http://link.aps.org/doi/10.1103/PhysRevA.94.022337>.
- [61] Viola, L., Knill, E. & Lloyd, S. Dynamical decoupling of open quantum systems. *Phys. Rev. Lett.* **82**, 2417–2421 (1999). URL <http://link.aps.org/doi/10.1103/PhysRevLett.82.2417>.